RESEARCH ARTICLE

Hybrid vortex simulations of wind turbines using a three-dimensional viscous–inviscid panel method

Néstor Ramos-García[1] , Mads Mølholm Hejlesen[2], Jens Nørkær Sørensen[1] and Jens Honoré Walther[2,3]

[1] Department of Wind Energy, Technical University of Denmark, Building 403, Kgs. Lyngby DK-2800, Denmark
[2] Department of Mechanical Engineering, Technical University of Denmark, Building 403, Kgs. Lyngby DK-2800, Denmark
[3] Computational Science and Engineering Laboratory, ETH Zürich, Clausiusstrasse 33, Zürich CH-8092, Switzerland

ABSTRACT

A hybrid filament-mesh vortex method is proposed and validated to predict the aerodynamic performance of wind turbine rotors and to simulate the resulting wake. Its novelty consists of using a hybrid method to accurately simulate the wake downstream of the wind turbine while reducing the computational time used by the method. The proposed method uses a hybrid approach, where the near wake is resolved by using vortex filaments, which carry the vorticity shed by the trailing edge of the blades. The interaction of the vortex filaments in the near vicinity of the wind turbine is evaluated using a direct calculation, whereas the contribution from the large downstream wake is calculated using a mesh-based method. The hybrid method is first validated in detail against the well-known MEXICO experiment, using the direct filament method as a comparison. The second part of the validation includes a study of the influence of the time-integration scheme used for evolving the wake in time, aeroelastic simulations of the National Renewable Energy Laboratory 5 MW wind turbine and an analysis of the central processing unit time showing the gains of using the hybrid filament-mesh method. Copyright © 2017 John Wiley & Sons, Ltd.

Correspondence
Néstor Ramos-García, Department of Wind Energy, Fluid Mechanics Section, Technical University of Denmark, Building 403, Kgs. Lyngby DK-2800, Denmark.
E-mail: nerga@dtu.dk

1. INTRODUCTION

In the recent years, vortex methods have become an attractive tool for the analysis and design of wind turbine rotors.[1] Combined with panel methods, the complete blade geometry is taken into account in the simulation after which a detailed aerodynamic description is obtained where sub-chord flow scales are included. The panel method uses a surface distribution of flow singularities to model the turbine rotor and thus avoiding complicated and computationally costly body-fitted meshing schemes. As a result, these solvers are of a higher fidelity than the lifting line method or the blade element momentum method[2] that at this point constitutes the industry standard.

Inherently, the panel method only solves the inviscid boundary conditions. In order to take viscous effects into account, the method must be combined with a viscous momentum equation. One method is to include a model based on the integral boundary-layer equations to create this viscous–inviscid coupling and thus obtain an approximated effect of a viscous boundary layer. In the literature, a number of different viscous–inviscid couplings for two-dimensional flows have been presented.[3–8]

In transient simulations, discrete vortex elements are released from the blade and transport the circulation of the flow. The trajectory of the discrete vortices is governed by the Biot–Savart interaction law. In aeroelastic simulations, an accurate calculation of the wake is essential; however, it can easily become computationally too expensive with the increasing

number of discrete vortex elements. Extensive work has been performed on developing vortex codes for wind turbine simulations using a variety of discrete vortex elements[9–16] for an unbounded domains also referred to as *free-wake* methods.

A direct interaction between all the N discrete vortex elements of the flow have a computational scaling of N^2. Hence, more efficient methods are needed in order to perform simulations of a well-resolved wake. Common strategies for obtaining an increased efficiency is either to significantly reduce the number of discrete elements by grouping elements into fewer data points or to construct a more favorable data structure in order to obtain an effective calculation of the interaction. The former strategy is utilized in the fast multipole method[17] based on tree algorithms[18] where high-order multipole expansions are used to reduce the number of interacting elements. The latter strategy is utilized in hybrid particle-mesh (PM) methods[19] where discrete particles are interpolated onto a uniform mesh. This enables the use of fast recursive algorithms such as the fast Fourier transform (FFT) to efficiently compute the particle interactions that in this case consist of solving the Poisson equation subject to free-space boundary conditions. A high-order regularization method for solving the Poisson equation in the PM scheme is proposed by Hejlesen *et al.*[20–22] to obtain an arbitrary high order of convergence.

Recently, MIRAS (Method for Interactive Rotor Aerodynamic Simulations) was developed by Ramos-García *et al.*[23, 24] Here, a three-dimensional (3D) panel method is used to simulate the rotating blades of a wind turbine. The method uses a surface distribution of quadrilateral sources and doublets and is coupled to an integral boundary-layer solver that accounts for the viscous effects, including Coriolis and centrifugal forces, in the vicinity of the blade surface. MIRAS simulates the vortex shedding of the wind turbine rotors using a sheet of vortex filaments whose interaction is calculated by a direct filament–filament calculation (DM) at a low-computational efficiency. The presented hybrid filament-mesh implementation is an extension of the MIRAS code with the high-order mesh-based Poisson solver of Hejlesen *et al.*[20–22] This extension aims at significantly increasing the computational efficiency while maintaining the accuracy of the original direct method.

The paper is organized as follows. In Section 2, the hybrid filament-mesh vortex method is presented together with the applied panel method using a viscous–inviscid boundary-layer model. Validation of the direct filament method and the hybrid filament-mesh method is provided in Section 3 together with a time scheme analysis, an aeroelastic validation and a central processing unit (CPU) time study of the new method. Conclusions are presented in Section 4.

2. METHODOLOGY

In the proposed hybrid filament mesh, the wake behind a wind turbine is divided into two regions, a near-wake and a far-wake region. The vorticity that is shed by the blades is carried by discrete vortex filaments in the form of circulation. The interaction of the filaments is calculated by a direct calculation for filaments in the near-wake region and by a mesh method for filaments in the far-wake region. A visualization of the simulated flow past the MEXICO rotor using the hybrid method is shown in Figure 1. In the figure, the vorticity in near-wake region is visualized by a wire-frame representation of the released vortex filaments, while in the far-wake region, the vorticity is visualized using an iso-contour of its magnitude on the mesh. In the paper, the terms near and far wake are defined in relation to the applied modeling approach. Therefore, the near wake is the region modeled with the direct filament–filament interaction, while the far wake is modeled by the PM approach.

The vorticity is released from the rotor downstream at the trailing edges of the blades. This is performed by a single row of quadrilateral doublet panels/rings following the bisector of the upper and lower trailing edge panels, at the different blade sections. As discussed by Katz and Plotkin,[25] the relatively large distance from the blade trailing edge of an equivalent discrete vortex panel/ring compared with the small distance of a continuous wake causes a wake-discretization error which underestimates the induced velocity. A typical numerical approach to correct for this error is to convect the first row of wake panels/rings with 30% of the local undisturbed velocity.

This row of wake panels is used to satisfy the Kutta condition (Section 2.3). Downstream from this row, the quadrilateral doublets are transformed into straight-line vortex filaments, grouped in vortex ring elements, which are formed by four interconnected filaments. The circulation of these vortex filaments remains constant in time with their motion being described by Lagrangian filament markers placed at their end points.

The trajectory of the filaments is determined by the velocity of the filament markers $u(x_i)$, which in turn is calculated by a superposition of the free-stream velocity V_0 and the velocity contributions from all filaments and boundary elements at the position of the filament marker x_i.

$$\frac{dx_i}{dt} = u(x_i) \qquad \text{with} \qquad u(x_i) = V_0 + u_\sigma(x_i) + u_{\text{ff}}(x_i) + u_{\text{fm}}(x_i) \tag{1}$$

Here, u_σ is the velocity induced by the blade source elements including the aforementioned row of wake panels. u_{ff} and u_{fm} are the velocities induced by the vortex filaments of the near-wake (filament to filament) and far-wake regions (mesh to filament), respectively. Vortex filaments that leave the Cartesian mesh are removed from the simulation. Different time-integration schemes have been implemented for solving the trajectory equation of the filaments. Some of these
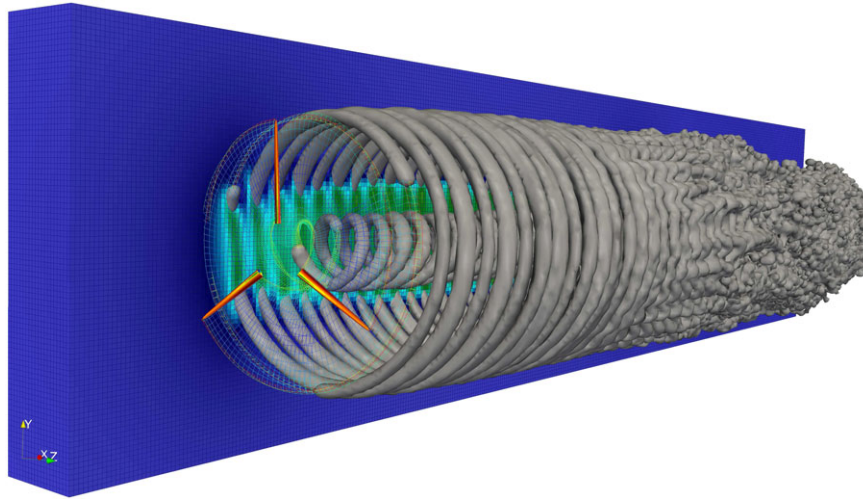
Figure 1. Visualization of the flow past the MEXICO rotor at 15 m s^1 simulated with the hybrid filament-mesh method. The filaments whose interactions are calculated by a direct filament–filament calculation are depicted by a wire frame, and filaments whose interaction is calculated by a mesh are depicted by the iso-surface of the vorticity magnitude on the mesh. [Colour figure can be viewed at wileyonlinelibrary.com]

methods are tested in Section 3.3. The calculation of the different velocity contributions of equation (1) will be explained in detail in the following.

2.1. The direct calculation of the filament interaction

The near-wake velocity contribution, $\boldsymbol{u}_{\text{ff}}$, is obtained directly by evaluating the Biot–Savart law and summing the velocity induced by all filaments that form the near wake. A regularized Biot–Savart law is applied by introducing a finite vortex core to avoid a singular interaction between filaments.

$$\boldsymbol{u}_{\text{ff}}(\boldsymbol{x}_i) = \sum_{j=1}^{N_{\text{ff}}} K_{ij} \frac{\gamma_j}{4\pi} \frac{\boldsymbol{t}_j \times \boldsymbol{r}_{ij}}{r_{ij}^3} \qquad \text{where} \qquad K_{ij} = \frac{r_{ij}^2}{\left(\varepsilon_j^{2z} + r_{ij}^{2z}\right)^{1/z}} \tag{2}$$

$\boldsymbol{r}_{ij} = \boldsymbol{x}_i - \boldsymbol{y}_j$ is the distance vector from the vortex element $\boldsymbol{y}_j$ to the evaluation point $\boldsymbol{x}_i$, $r_{ij} = |\boldsymbol{r}_{ij}|$. γ_j is the circulation of the filament, and $\boldsymbol{t}_j$ is the unit orientation vector of the jth filament. ε_j is the vortex core radius of the filament, and z defines the cutoff velocity profile where the Scully profile,[26] $z = 1$, has been used in this work.

In the direct filament–filament calculations, a viscous core model is applied to emulate the effect of viscosity by changing the vortex core radius as a function of time.[27] In this way, the vortex core radius is integrated in time according to

$$\varepsilon_i(t) = \sqrt{4\alpha_v \delta_v \nu t_i} + \varepsilon_0 \tag{3}$$

Here, α_v is a constant set to 1.25643,[28] δ_v is a turbulent eddy viscosity parameter proposed by Squire,[29] here set to 10^{-3}, ν is the kinematic viscosity and t_i is the time elapsed since the generation of the ith filament. To avoid the singular behavior for newly released vortex elements, an initial core radius, ε_0, is introduced.

2.2. The hybrid filament-mesh calculation of the filament interaction

The far-wake velocity contribution, $\boldsymbol{u}_{\text{fm}}$, is obtained by transforming the circulation of the filaments into a vorticity distribution on a uniform Cartesian auxiliary mesh where the interaction is efficiently calculated by an FFT-based method. The transformation from filaments to mesh is performed in two steps as depicted in Figure 2.

In the first step, the filaments are translated into particles. The integral vorticity vector of the generated particles, $\boldsymbol{\xi}_{\text{p}}$, is computed from the filament circulation, Γ, by

$$\boldsymbol{\xi}_p = \left(\frac{\Gamma_i l_i}{n_{\text{p}}}\right) \boldsymbol{t}_i \qquad \text{where} \qquad n_{\text{p}} = \text{ceiling}\left(\frac{l_i}{h}\right) \tag{4}$$
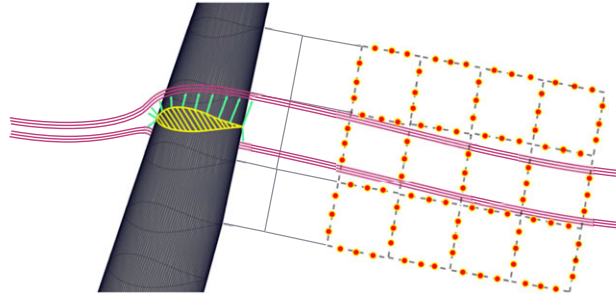
Figure 2. Sketch of the hybrid method in the vicinity of the blade. The initial gray mesh downstream the blade trailing edge represents the region of the direct-filament interaction, the red dots represent the particles generated when interpolating from the vortex filament to the mesh, and the cyan vectors represent the source distribution used to mimic the presence of a viscous boundary layer. [Colour figure can be viewed at wileyonlinelibrary.com]

Here, l_i is the filament length, t_i is the tangential unitary vector of the ith filament and n_p is the minimum number of particles required to ensure a continuous vorticity field on the mesh and is determined by the round-up integer of dividing l_i by the mesh cell size h. The location of the generated particles are then distributed along the filament.

$$x_p = \left(1 - \frac{p}{n_p + 1} \right) x_i + \frac{p}{n_p + 1} x_j \qquad \text{where} \qquad p = \{1, 2, \ldots, n_p\} \tag{5}$$

Here, x_i and x_j denotes the position of the two filament markers and x_p the position of the n_p generated particles for the filament in question.

In the second step, the generated particles are interpolated onto the mesh. As the particles now represent an integral of the vorticity, the vorticity field $\omega(x_m)$ can be reconstructed on the mesh points x_m by utilizing the superposition principle for the n_p particles.

$$\omega(x_m) = \frac{1}{h^3} \sum_p^{n_p} \xi_p \, W\left(\frac{x_p - x_m}{h} \right) \tag{6}$$

Here, h is the mesh cell width and $W(x)$ is the interpolation kernel that is composed of one-dimensional interpolation kernels for each direction as $W(x) = M(x)M(y)M(z)$. In this work, the interpolation kernel used is the third-order B-spline of Monaghan.[30]

Once the vorticity field has been constructed on the mesh, the velocity field is calculated by a Poisson equation that may easily be inverted and solved in Fourier space.

$$\nabla^2 u = -\nabla \times \omega \qquad \Rightarrow \qquad \hat{u} = \iota k \times \left(\frac{\hat{\omega}}{k^2} \right) = \iota k \times \left(\hat{G} \hat{\omega} \right) \tag{7}$$

Here, the $\hat{\ }$ denotes a Fourier transformed variable, $k = (k_x, k_y, k_z)$ is the angular wave number of the Fourier space and $k^2 = k_x^2 + k_y^2 + k_z^2$. Hence, the solution depends on defining an appropriate Green's function G.

To obtain free-space boundary conditions, the Green's function needs to be regularized in order for the solution to be bounded in Fourier space, thus avoiding errors in the inverse FFT that is needed to retrieve the solution in real space.[20] Following Hejlesen *et al.*,[21] an eight-order regularized Green's function is used, which in real space is given by

$$G(\rho) = \frac{1}{4\pi \, \varepsilon_m \, \rho} \left(\frac{1}{\sqrt{2\pi}} \left(\frac{19}{8} \rho - \frac{2}{3} \rho^3 + \frac{1}{24} \rho^5 \right) \exp\left(-\frac{\rho^2}{2} \right) + \mathrm{erf}\left(\frac{\rho}{\sqrt{2}} \right) \right) \quad \text{where} \quad G(0) = \frac{35}{64} \frac{\sqrt{2}}{\pi^{3/2} \varepsilon_m} \tag{8}$$

Here, $\rho = r/\varepsilon_m$ is the radial distance normalized by a regularization radius ε_m analogous to the vortex core of the direct method. The regularization radius is here chosen as $\varepsilon_m = 1.5 \, h$ in order to minimize the smoothing error of the regularization[20, 21] and to obtain an effective vortex core that is close to that used in the direct filament–filament calculations.

Using this Green's function combined with the FFT-based free-space convolution method of Hockney and Eastwood,[19] the velocity field is obtained to an eight-order accuracy. The obtained velocity field is then interpolated back to the filament end markers in order to be included in equation (1) as the u_{fm} term.

$$u_{\mathrm{fm}}(x_i) = \sum_{m}^{N_{\mathrm{m}}} u(x_m)\, W\left(\frac{x_m - x_i}{h}\right) \tag{9}$$

Here, N_{m} is the number of mesh points within the support of the interpolation kernel.

2.3. The viscous–inviscid panel method

The rotor blades are modeled by a surface distribution of quadrilateral doublets, with strength μ_j and quadrilateral sources with strength σ_j to enforce a blade surface that is impermeable to the flow. An extra source distribution, ϕ_j, is used to model the viscous effects confined inside the boundary layer employing the transpiration velocity concept,[31] which can be considered as an outflow because of the boundary-layer growth. This is calculated using the viscous–inviscid implementation Q^{3}UIC,[32] which is based on solving the quasi-3D integral boundary-layer equations. Enforcing these boundary conditions at the blade surface gives a system of equations that is closed by including the Kutta condition.

$$B_{ij}\left(\sigma_j + \phi_j\right) + \left(A_{ij} + C_{ij}\right)\mu_j = -\left(V_0 + \Omega \times r_i + v_i + u_{\mathrm{ff}}(x_i) + u_{\mathrm{fm}}(x_i)\right) \cdot n_i \tag{10}$$

Here, B_{ij} is the normal induction matrix of a quadrilateral unitary source distribution and A_{ij} is the normal induction matrix of a unitary quadrilateral doublet. C_{ij} is the normal induction matrix of a unitary wake quadrilateral doublet, having only non-zero values for panels that form part of a blade trailing edge. The sign of C_{ij} depends on whether the inducing panel is on the upper or on the lower side of the trailing edge. Ω is the angular velocity of the blade, and v_i is the velocity of the blade caused by structural deformation. r_i is the radial position, and n_i is the unit normal vector of the ith panel. The quadrilateral sources σ_j have been given a value equal to the normal component of the undisturbed velocity at the center of each quadrilateral panel to ensure the uniqueness of the system. To satisfy the unsteady Kutta condition of zero loading in trailing edge, a row of quadrilateral doublet distributions is released from the blade trailing edges, modeling the vorticity released by the blades. Its strength is equal to the difference between the upper and lower trailing edge panel doublets along the span-wise direction.

The local angle of attack at each blade span-wise section, α, is used to couple the integral boundary-layer equations and the 3D panel method. In the coupling, the transpiration velocity concept is used to modify the Neumann no penetration boundary condition around the solid body. The transpiration velocity is obtained by integrating the continuity equation across the boundary layer following,[31]

$$w_T = \frac{\partial}{\partial s}\left(u_e \delta_1^*\right) \tag{11}$$

where u_e is the edge velocity and δ_1^* denotes the displacement thickness.

Q^{3}UIC is used to compute the boundary-layer integral parameters needed to obtain the chord-wise distribution of the transpiration velocity at each span-wise station and the data is stored in a data file. In the 3D panel method, the angle of attack at each cross section is calculated and the corresponding chord-wise transpiration velocity distribution, w_T, is obtained from the previously created data file. The computed local chord-wise variation of the transpiration velocity is introduced in the 3D panel method as an additional source distribution, ϕ_j. For a more detailed explanation of the interactive viscous–inviscid coupling, the reader is referred to Ramos-García *et al.*[23]

Thwaites' method is employed to solve the laminar flow regions,[33] whereas the turbulent flow is modeled using the integral form of the quasi-3D $r-$ and $\theta-$ momentum equations. In addition, the kinetic energy shape parameter equation is implemented to allow for variations from turbulent equilibrium flows. Laminar to turbulent transition can be both prescribed by the user or predicted by the e^n envelope method with Mack's modification to account for the inflow turbulence intensity level.[34] A strong coupling between the viscous and inviscid parts is used, making the solver capable to overcome the Goldstein's singularity and therefore solve the boundary-layer equations up to and through mild flow separation regions.

The aerodynamic forces on the blades are calculated by the surface pressure distribution, C_{p}, which in turn is computed by applying the unsteady Bernoulli equation. It is assumed that the time variation of the velocity potential is equal to the local time variation of the doublet distribution at each panel. Hence, the resulting pressure coefficient C_{p} is given by

$$C_{\mathrm{p}}(x_i) \equiv \frac{p - p^*}{\frac{1}{2}\rho\left|v_i^*\right|^2} = 1 - \frac{|u(x_i)|^2}{\left|v_i^*\right|^2} - \frac{2}{\left|v_i^*\right|^2}\frac{\partial\mu}{\partial t} \tag{12}$$

where p^* is the reference pressure in the far-field and $\boldsymbol{v}_i^*$ is the reference velocity at panel i given by

$$\boldsymbol{v}_i^* = -(\boldsymbol{V}_0 + \Omega \times \boldsymbol{r}_i + \boldsymbol{v}_i) \tag{13}$$

The local force $\Delta\mathbf{F}$ applied on a panel with area $\Delta\mathbf{S}$, is calculated as

$$\Delta\mathbf{F} = -C_p \left(\frac{1}{2}\rho \left|\boldsymbol{v}_i^*\right|^2\right) \Delta\mathbf{S} \cdot \mathbf{n} \tag{14}$$

where $\mathbf{n}$ is the normal outward pointing unitary vector of the specific panel. The normal and tangential components of the aerodynamic forces on the blade are computed by adding the contributions from each panel in the global coordinate system, including the influence of the friction drag obtained with the boundary-layer solver.

3. NUMERICAL RESULTS

3.1. Validation of the direct method using filament–filament calculations only

A validation of the method using only the direct filament–filament interaction is carried out to set a baseline for the comparison with the hybrid filament-mesh method. Although earlier publications by the authors have included a general validation of the MIRAS code,[23, 24] the present validation focuses on the effect of the wake calculations. Furthermore, a recent parallelization of the code makes it possible to perform a convergence study for finer wake discretizations. This is essential in aeroelastic simulations as the azimuthal wake resolution has to be in the order of 1° to correctly capture the turbine aeroelastic modes, or higher frequency perturbations like the tower shadow effect.

The blade resolution used in all the cases presented in this article consists of 20 span-wise and 150 chord-wise stations, with a total of 3000 cells. Convergence studies on the body discretization have been previously presented in Ramos-García *et al.*[23] It was found that a 20 panel span-wise discretization was sufficient to ensure convergence of the aerodynamic forces in the blade; however, a larger number of chord-wise panels (≥ 100) was necessary to attain convergence in the tangential component of the force. As stated earlier, the validation of the direct method has been included as a reference for the comparison with the hybrid filament-mesh method. Because of the nature of the direct Biot–Savart problem, whose complexity squares with the number of vortex elements, a further increase in the span-wise resolution would make the finer azimuthal wake resolution cases very computationally expensive, and therefore, higher span-wise resolutions have not been included in the present validation.

As a benchmark, the MEXICO rotor has been selected for the present validation. The available experimental data for the MEXICO rotor includes rotor forces obtained from balance measurements and surface pressure distributions measured with a set of Kulite pressure sensors positioned along four different span-wise stations on the blade. Furthermore, the wake was characterized in detail by using particle image velocimetry (PIV) measurement technology. The three-bladed MEXICO rotor has a diameter of 4.5 m, rotates with a constant angular speed of 424.5 rpm at wind speeds of 10, 15 and 24 m s^1.
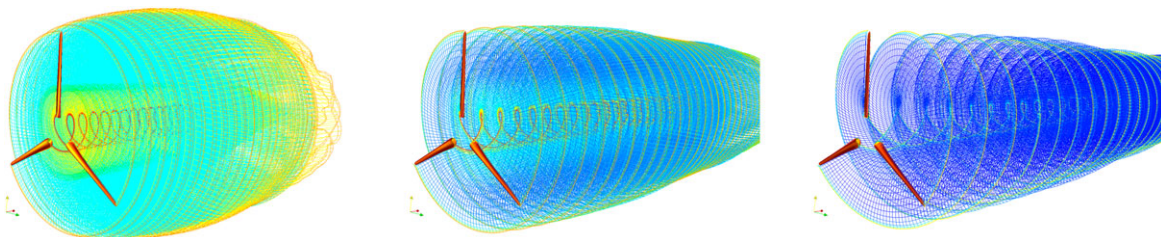

Figure 3. MIRAS DM simulation for an azimuthal wake discretization of 2.5°, at a wind speed of 10 m s^1 (left), 15 m s^1 (center) and 24 m s^1 (right). [Colour figure can be viewed at wileyonlinelibrary.com]

Table I. MEXICO rotor, simulation test cases.

Wind speed (m s^1)	Omega (rad s^1)	Tip speed ratio	Simulation time (s)	No. of wake revolutions	Free-stream displacement (m)
10.00	44.45	10.00	4.24	30	42.40
15.00	44.45	6.67	2.83	20	42.40
24.00	44.45	4.17	1.84	13	42.40

The blades are subjected in the three cases to a collective pitch of $-2.3°$. Instantaneous velocities were extracted in a plane at 9 o'clock when looking downstream at the rotor when the first blade pointed upwards. For more detailed information about the MEXICO experimental campaign, the reader is referred to Schepers and Snel.[35]

The validation is performed for the MEXICO rotor at wind speeds of 10, 15 and 24 m s[1], with corresponding tip speed ratios 10.00, 6.67 and 4.17. The flow is simulated for 4.24, 2.83 and 1.84 s, respectively, which is equivalent to solving 30 wake revolutions for the 10 m s[1] case, 20 wake revolutions at 15 m s[1] and 13 wake revolutions at 24 m s[1]. The number of wake revolutions has been chosen to attain a steady solution where the further development of the wake does not affect the rotor loading nor the flow in the rotors vicinity. Visualizations of the simulated wakes are presented in Figure 3. The three test cases are summarized in Table I. As can be appreciated in the succeeding figures, the most inner part of the blade, defined with a cylindrical profile, has not been included in the blade surface generation.

Six different wake resolutions of, respectively, 20.0°, 10.0°, 5.0°, 2.5°, 1.25° and 0.625° azimuthal discretization have been employed in the study. For the cases of 10 and 15 m s[1], the minimum resolution was set to 2.5° and 1.25°, respectively.

Initial simulations showed that the tip vortex does not roll up for the coarse resolutions. This was found to be related to the initial vortex core radius of the filament ε_0 that initially was set to 10% of the chord, following previous studies. To obtain a convergence of the flow characteristics downstream the turbine, it was found that ε_0 (equation (3)) should be of the same order of magnitude as the boundary-layer thickness. This especially applies in the region where the tip vortex is generated. The boundary-layer thickness is approximated as $\delta = c/\sqrt{Re}$, where c is the local airfoil chord. For the simulations presented in this work, ε_0 has been approximated to 0.1% of the local chord, which is of the same order of magnitude as the boundary-layer thickness at the trailing edge of the blade.

The error in the predicted rotor thrust and torque has been analyzed and summarized in the convergence study presented in Table II. The reported errors are relative to results predicted at the finest wake resolution. The errors show a reasonable convergence for the lower wind speed cases. A second-order convergence is obtained for the 10 m s[1] case, while a first-order convergence is found at 15 m s[1]. The convergence trend is not as clear for the 24 m s[1] simulations; however, it is seen that the error is generally smaller than at the lower wind speeds.

The blade loading computed in the direct filament method simulations for the finest wake discretization is compared with experimental data of the MEXICO experiment in Figure 4. It has been observed that the tip and root regions are more sensitive to the wake discretization (not shown). This is a consequence of the vortex roll-up, which is directly affected by the azimuthal wake discretization. Compared with the experimental values, there is a general tendency to underpredict the loading in the root region. This can be explained by the underprediction of the rotational effects arising from the Coriolis and centrifugal forces inside the boundary layer. Such forces act generating an outward flow that reduces the boundary-layer thickness and hence the viscous effects of the flow, which causes an increase of the normal force component and a reduction

Table II. Error in the prediction of rotor thrust and torque using the direct-filament method.

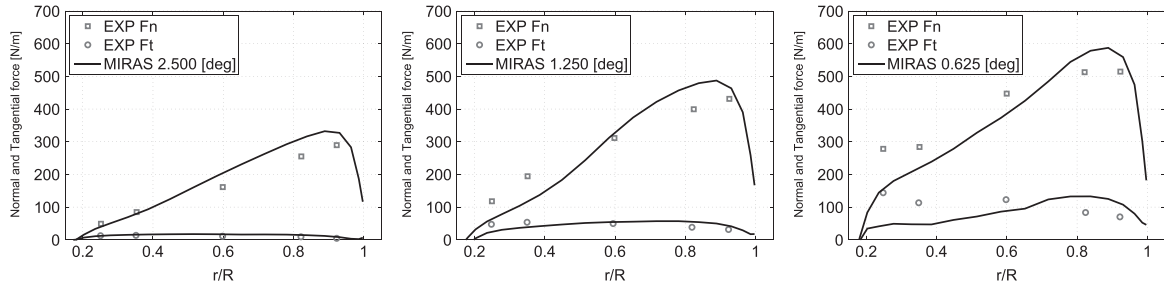| Wind speed (m s[1])	$d\theta$ (°)	Number of filaments (—)	Error in thrust (%)	Error in torque (%)
10.00	20.000	63,180	5.19	11.84
	10.000	126,360	1.99	3.67
	5.000	252,720	0.48	0.38
	2.500	505,440	—	—
15.00	20.000	42,120	2.31	5.39
	10.000	84,240	1.08	2.42
	5.000	168,480	0.52	1.23
	2.500	336,960	0.19	0.51
	1.250	673,920	—	—
24.00	20.000	27,380	0.98	0.53
	10.000	54,760	0.04	1.11
	5.000	109,500	0.18	0.73
	2.500	219,000	0.01	0.14
	1.250	438,000	0.24	0.23
	0.625	876,100	—	—

Figure 4. Blade normal and tangential forces at a wind speed of 10 m s[1] (left), 15 m s[1] (center) and 24 m s[1] (right).
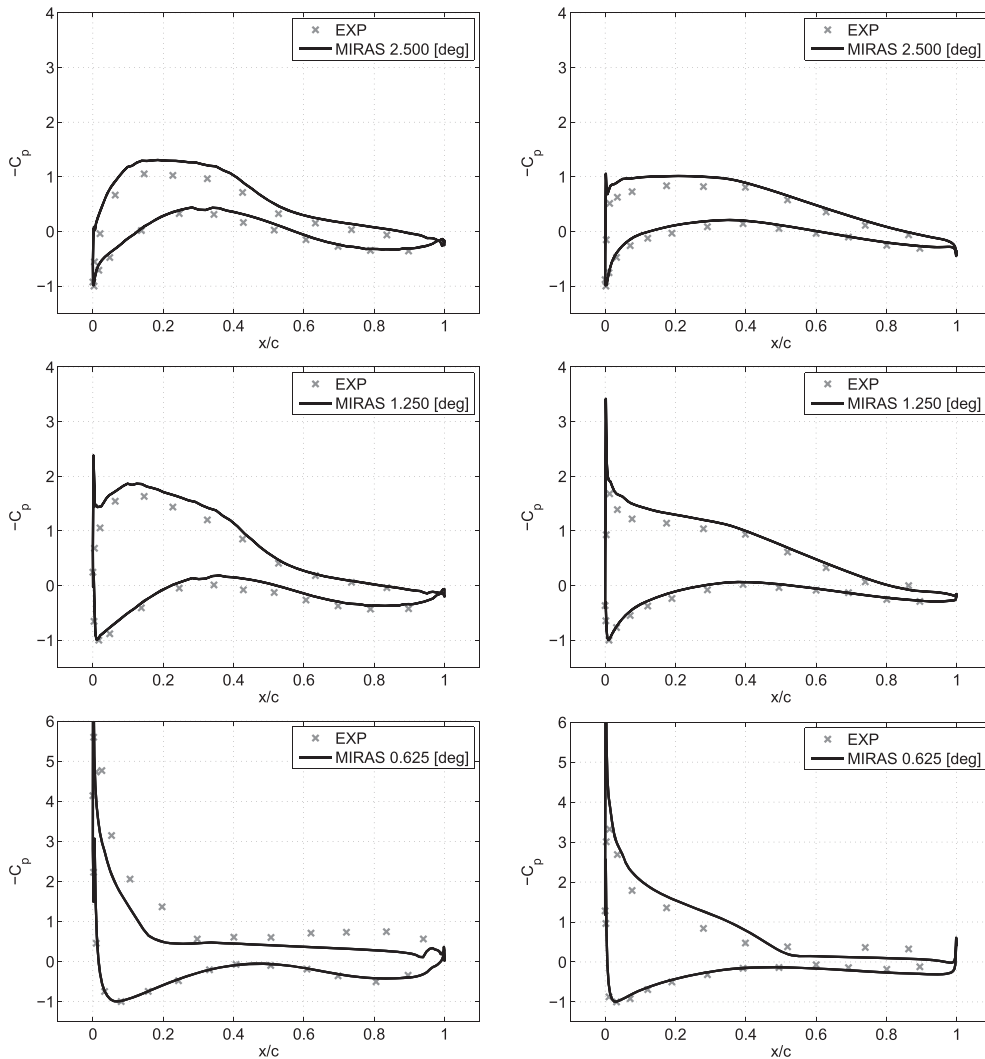

Figure 5. Surface pressure coefficients at different span-wise stations (in order from left to right and upper to lower) $0.60R$, $0.92R$, $0.60R$, $0.92R$, $0.35R$ and $0.82R$ at a wind speed of 10 m s[1] (upper), 15 m s[1] (middle) and 24 m s[1] (lower).

of drag. Moreover, there is an overprediction in the tip region, in accordance with what was observed during the MEXICO project[36] for a large variety of flow solvers, including a wide range of Navier–Stokes codes.

The calculated surface pressure distribution is analyzed and compared with experimental data in what follows. The distributions shown in Figure 5 are selected as representative of the three wind speed cases and four span-wise stations,

0.35*R*, 0.60*R*, 0.82*R* and 0.92*R*, for which experimental pressure tap data are available. In general terms, the MIRAS simulations overpredict the pressure in the suction side and in the outer part of the blade. A pressure underprediction is seen in the suction side of the root region, specially at 24 m s[1] (Figure 5) where 3D effects are not well captured by the quasi-3D boundary-layer solver, which predicts the separation location to be further upstream. The pressure side is in general well captured by the solver. The largest variations between the different wake refinements were observed in the trailing edge region.

Four cases are selected to study the influence of the wake resolution. The axial, radial and tangential components of the velocity are analyzed for the different wind speeds in the radial direction from 0.0 to 3.0 m, at a downstream location of 0.3 m from the rotor plane. The results are shown in Figure 6. A fast convergence is observed in the intermediate region, whereas the regions related to the tip and root of the blade experience a slower convergence. This is due to the need of a higher azimuthal discretization in order to resolve the complex flow dynamics caused by the tip and root of the blade. The code is not capable of predicting the steep gradients in the tangential velocity captured by the PIV technique. As reported by Schepers *et al.*,[36] this behavior was neither captured by any of the codes employed during the Mexnext blind comparison, which included a variety of high-fidelity computational fluid dynamics solvers.

The axial transverse-simulated velocities for the 15 m s[1] wind speed case are compared in Figure 7. The velocities are sampled at a radial distance of 1.377 m from the rotor axis at a distance of 6.0 m upstream to 6.0 m downstream of the rotor plane. Here, it is seen that the amplitude of the variations is significantly reduced for the high resolutions (i.e., small $d\theta$). In comparison with the experimental PIV measurements, the direct-filament calculations tend to overpredict the axial velocity component downstream the rotor plane, showing a lower axial induction factor. It is seen that the agreement of the variations in the radial component of the velocity seems to be improved by refining the wake. The variations in the tangential component, however, do not show a similar agreement.

The axial, radial and tangential components of the velocity predicted by the solver using a larger initial vortex core radius (10 % of the local chord) are presented in Figure 8. As stated earlier, it is clear from the figure that convergence of
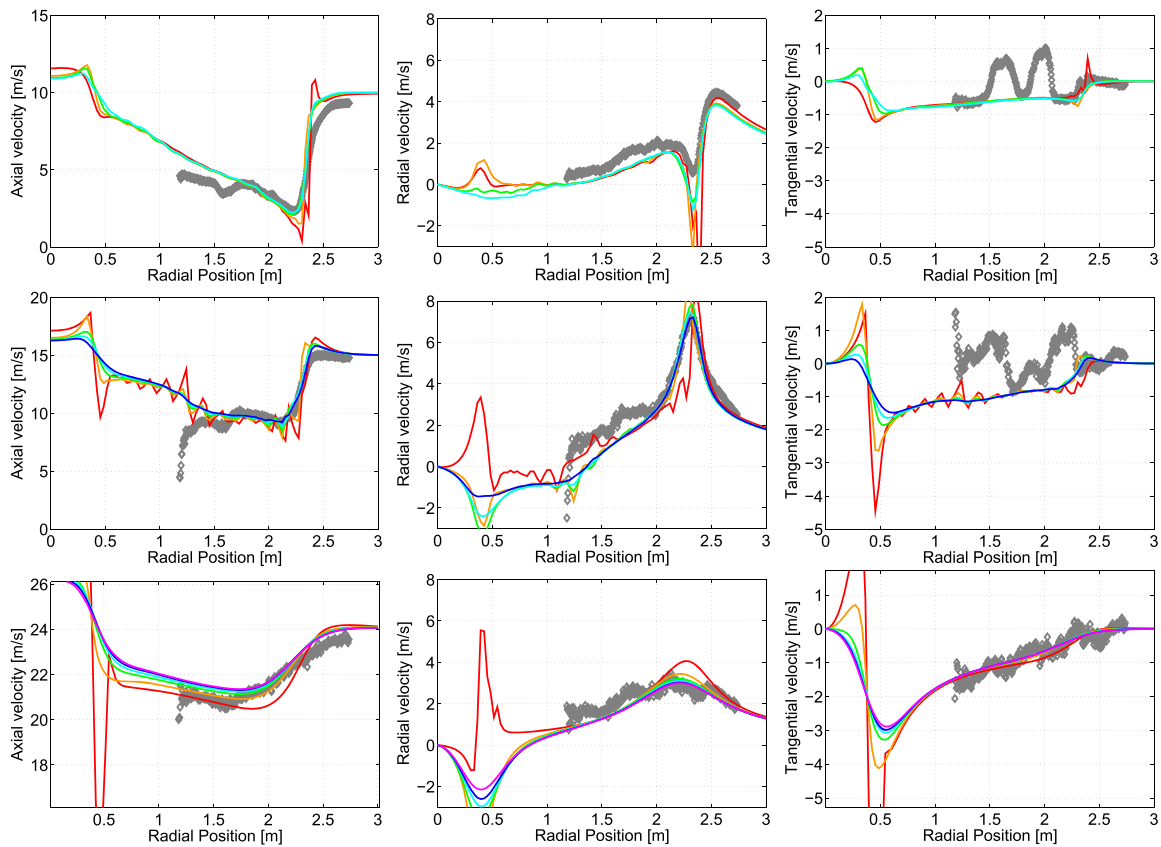

Figure 6. Axial (left), radial (center) and tangential (right) velocities along the radial traverse at a wind speed of 10 m s[1] (upper), 15 m s[1] (middle) and 24 m s[1] (lower). ◆, PIV[35]; ——, $d\theta = 20.000$; ——, $d\theta = 10.000$; ——, $d\theta = 5.000$; ——, $d\theta = 2.500$; ——, $d\theta = 1.250$; ——, $d\theta = 0.625$. [Colour figure can be viewed at wileyonlinelibrary.com]
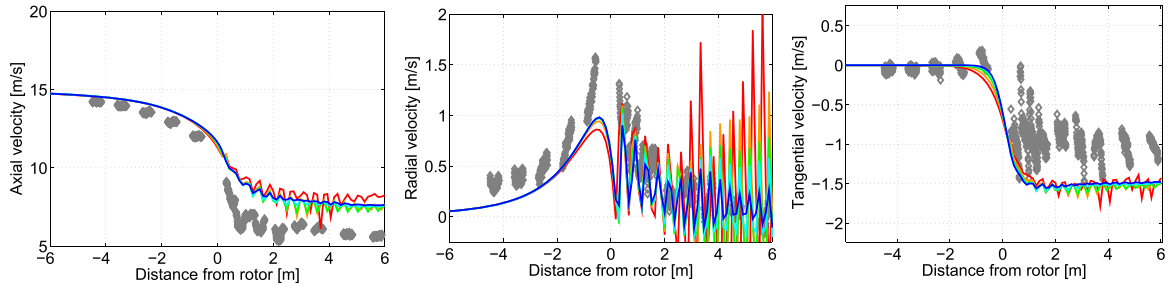
Figure 7. Axial (left), radial (center) and tangential (right) velocities along the axial traverse, at a wind speed of 15 m s[1]. ♦, PIV[35]; —, $d\theta = 20.000$; —, $d\theta = 10.000$; —, $d\theta = 5.000$; —, $d\theta = 2.500$; —, $d\theta = 1.250$. [Colour figure can be viewed at wileyonlinelibrary.com]
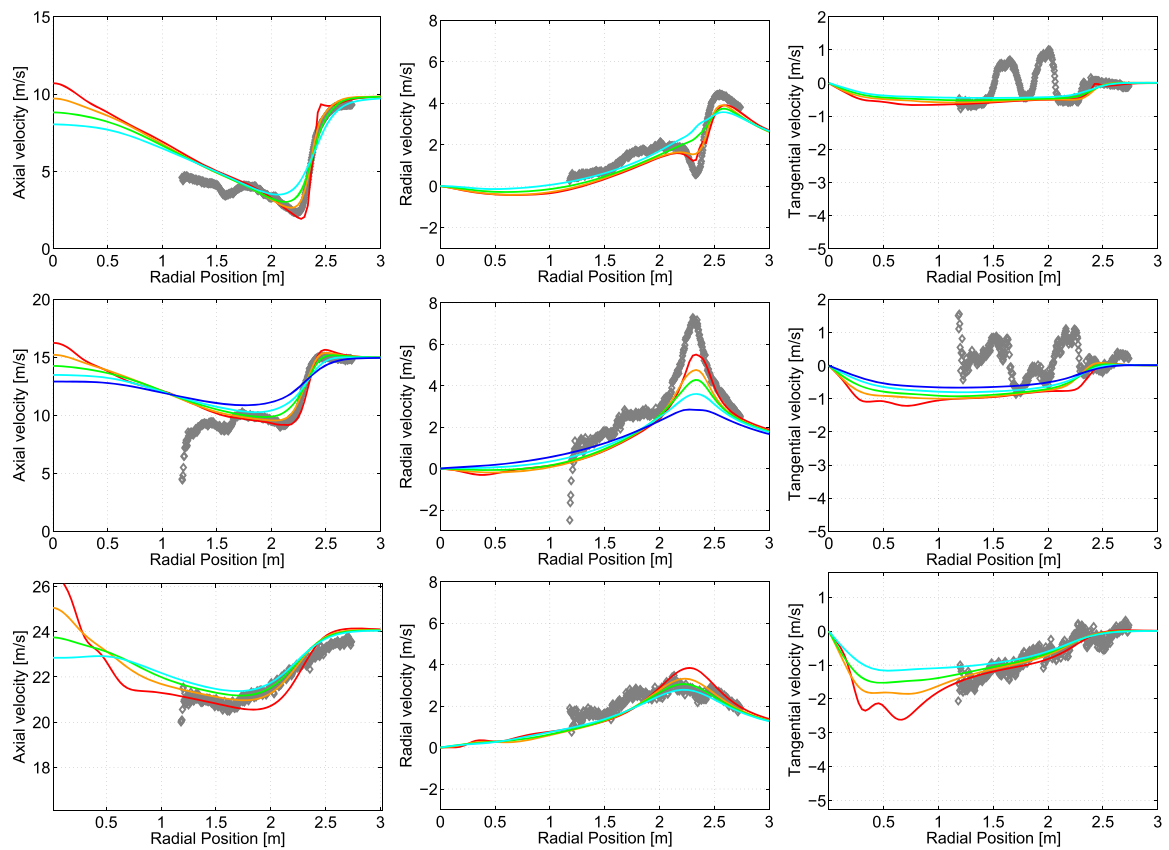

Figure 8. Axial (left), radial (center) and tangential (right) velocities along the radial traverse at a wind speed of 10 m s[1] (upper), 15 m s[1] (middle) and 24 m s[1] (lower) for an initial viscous core radius of 10% the local chord. It is clearly seen how convergence is not achieved for such a initial core radius. ♦, PIV[35]; —, $d\theta = 20.000$; —, $d\theta = 10.000$; —, $d\theta = 5.000$; —, $d\theta = 2.500$; —, $d\theta = 1.250$. [Colour figure can be viewed at wileyonlinelibrary.com]

the predicted velocities is not achieved with the refinement in the azimuthal wake discretization. This effect is especially strong in the tip vortex region. Simulations with a coarser wake discretization are in better agreement with measurements; however, this is not relevant since convergence is not attained with the increase in number of wake elements. It is therefore recommended to use a smaller initial core radius as previously stated.
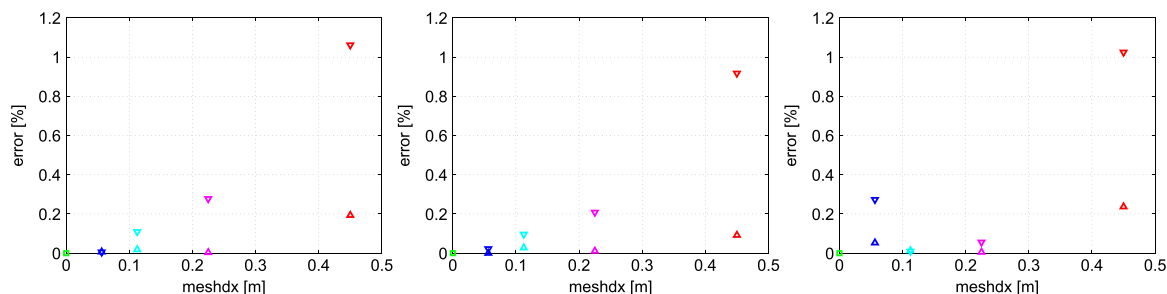
Figure 9. Error analysis of the thrust (up-pointing triangles) and torque (down-pointing triangles) predicted by MIRAS using the hybrid wake model with four different mesh resolutions for flows past the MEXICO rotor at a wind speed of 15 m s[1], after 5 (left), 10 (center) and 20 (right) wake revolutions. [Colour figure can be viewed at wileyonlinelibrary.com]

3.2. Validation of the hybrid implementation using the filament-mesh method

The hybrid implementation is here validated against the direct method of Section 3.1 and the experimental data for the MEXICO rotor.[35] As explained previously in Section 2, the filament-mesh method is implemented to increase the computational efficiency when calculating the velocity field induced by the filaments in the far wake. The direct method is applied in the vicinity of the rotor in order to avoid the additional smoothing error imposed by the cell size of the mesh.

Including the filament-mesh calculations evidently introduces an additional simulation parameter into the method, i.e., the mesh cell size h, which in turn is replaced with the regularization radius ε, compare with Section 2.2. This introduces an additional restricting length scale into the simulation where only flow scales above the regularization radius can be resolved. Evidently, choosing ε to be much smaller than the smallest filament length would render the effect of introducing a mesh inconsequential. This however would come at a great computational expense, and thus, a middle ground is sought where both efficiency and accuracy are obtained. Thus, a thorough study of the error introduced by different mesh resolutions is presented in order to validate the method.

Using the results of the direct method (cf. Section 3.1) as a benchmark, the error of the hybrid method is investigated for the 15 m s[1] case using a 5.0° azimuthal discretization of the filaments. The extent of the mesh is $5.5D \times 1.5D \times 1.5D$, with the rotor centered one diameter downstream from the mesh boundary compare with Figure 1. To analyze the influence of the mesh dimensions, simulations have been carried out for two larger meshes, ($10D \times 1.5D \times 1.5D$) and ($15D \times 2D \times 2D$), with no variation in the results (not shown).

The location at which the filament transitions from being included in the direct filament–filament calculation to being included in the filament-mesh calculation is prescribed by the number of wake revolutions (in degrees) the filament has undergone and is here denoted *startpmw*. In this study, *startpmw* is initially set to 20° but will be further investigated in the following.

The effect of the mesh resolution is investigated for four different resolutions $h = D/10, D/20, D/40$ and $D/80$ where the obtained error compared with the direct method is shown in Figure 9 for the calculated rotor thrust and torque at three different times characterized by 5, 10 and 20 wake revolutions.

Generally, a good convergence is observed with an error in thrust and torque below 0.3 % and 1.0 %, respectively for all the investigated mesh resolutions. A small divergence is however observed for the $D/80$ resolution after 20 wake revolutions, with a 0.05 % error in thrust and a 0.27 % error in torque. This divergence from the direct method may be related to a discrepancy between the vortex core of the filament in the direct filament–filament calculation and the regularization radius in the filament-mesh calculations.

In order to investigate the quality of wake dynamics for the hybrid method, the computed flow velocities along the axial and radial traverses are presented in Figure 10. It is here seen that the finest mesh resolution is necessary to accurately capture the local variation along the stream-wise direction of the three components of the velocity. Also, the mesh resolution is critical to capture the correct wake characteristics just downstream the rotor plane along the radial traverse. A mesh resolution of $D/80$ is necessary to accurately capture the velocities predicted by the direct-filament solver, especially the effect of the tip vortex in the radial component of the velocity.

Using the same benchmark case as earlier, the mesh resolution is now fixed to $h = D/40$ as the influence of the *startpmw* location is investigated for values 20°, 60°, 180° and 540°. The error in the torque after 5, 10 and 20 wake revolutions for the 15 m s[1] case is presented in Figure 11 for the four azimuthal discretizations. Here, it is seen that the error is of the order of $\mathcal{O}(10^{-3})$ for all cases and decreasing with increasing *startpmw*. The error of the calculated thrust prediction is observed in all cases to be approximately one order of magnitude smaller than the torque (not shown). Furthermore, the results suggest that for a high-wake resolution, a small *startpmw* may be used. This result should be noted as it may be used to reduce the computational time needed for the simulation compare with Section 3.5.
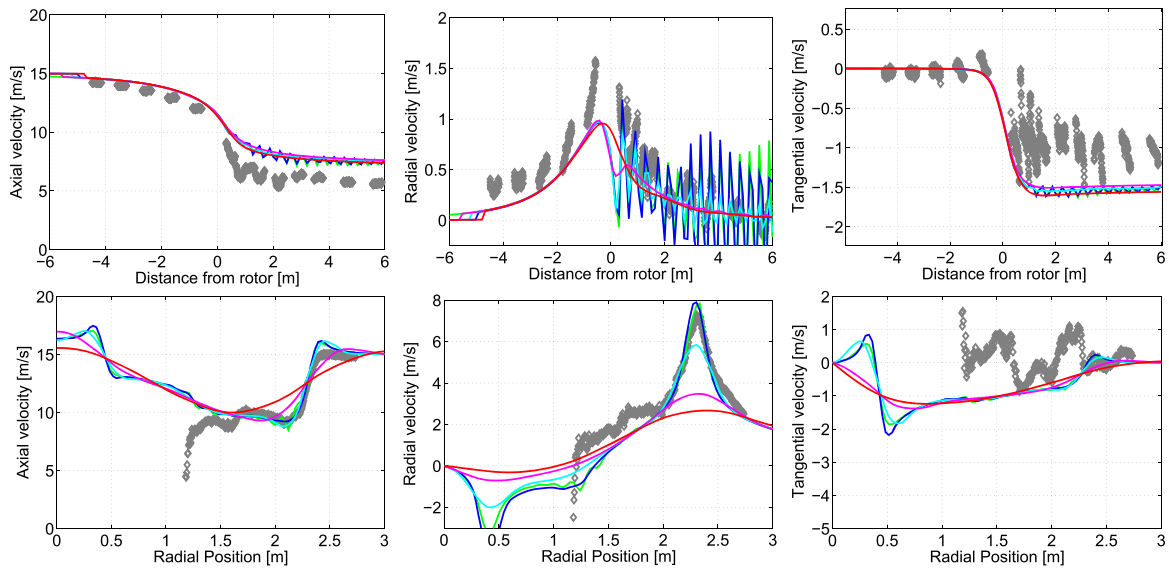
Figure 10. Axial (left), radial (center) and tangential (right) components of the velocity for four mesh discretizations (h) compared with PIV measurements and the direct-filament method at a wind speed of 15 m s[1] axial traverse (upper) and radial traverse (lower). ◆, PIV[35]; ——, DM; ——, $h = D/80$; ——, $h = D/40$; ——, $h = D/20$; ——, $h = D/10$. [Colour figure can be viewed at wileyonlinelibrary.com]
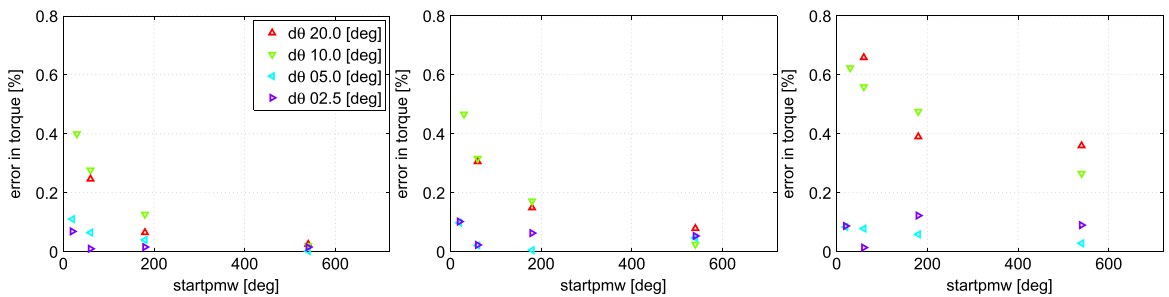

Figure 11. Error analysis of the torque predicted by the hybrid wake model as function of *startpmw* for flows past the MEXICO rotor at a wind speed of 15 m s[1], after 5 (left), 10 (center) and 20 (right) wake revolutions and four azimuthal discretizations. [Colour figure can be viewed at wileyonlinelibrary.com]

3.3. A study on the choice of time-integration scheme

The first-order Euler time scheme used for the previous validation is compared against the fourth-order predictor–corrector Adams–Bashforth–Moulton (ABM4). The analysis is performed for the flow past the MEXICO rotor at a wind speed of 15 m s[1]. The hybrid wake model is used in all cases with the *startpmw* parameter set to 20° and a mesh resolution of $h = D/40$. The error committed in the rotor thrust and torque predictions is analyzed.

Table III suggests that the error of the low-order Euler scheme is reduced by increasing the wake resolution. This trend is clearly seen in the torque predictions where the error using a 1.25° azimuthal wake discretization is decreased considerably, independently of the number of simulated wake revolutions.

Figure 12 shows vorticity iso-contour for three azimuthal wake discretizations, 10.0°, 2.5° and 1.25°, using the Euler and the ABM4 time schemes. In general, the ABM4 scheme seems more capable to capture some of the wake features in the far wake once instabilities take over and the structure of the wake breaks down, specially with a coarse wake discretization. In terms of the start location of such instabilities, both scheme predictions are in fairly good agreement for the finer wake resolutions. However, with a 10.0° or coarser azimuthal discretization, the Euler scheme predicts an upstream development of instabilities in comparison with the ABM4 predictions. In the 10.0° case, the wake instabilities using a Euler scheme start after approximately nine passes of the tip vortex structure while with the ABM4 scheme instabilities appear after 15 passes. Vortex leapfrogging is observed for the finer wake discretizations with both time schemes, although the lower-order scheme shows larger interactions between tip vortices. Closer to the rotor, differences in flow predictions between the two

Table III. Error in the prediction of rotor thrust and torque using a first-order Euler time-integration scheme for four different filament resolutions after 5, 10 and 20 wake revolutions. The error is calculated relative to predictions using the ABM4 time scheme for the same filament resolution and an equal number of wake revolutions.

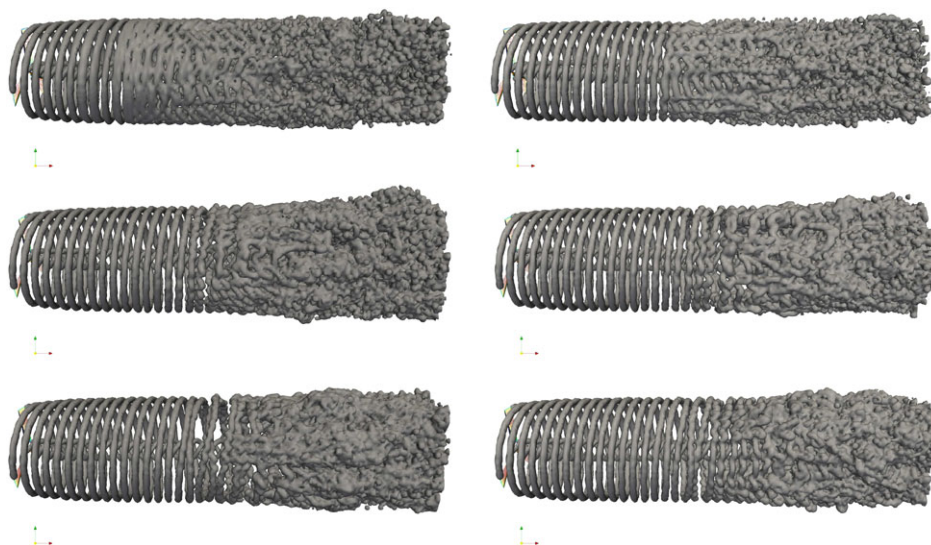| $d\theta$ (°)	Wake revolutions	Error in thrust (%)	Error in torque (%)
10.00	5	0.15	0.64
5.00	5	0.11	0.57
2.50	5	0.00	0.21
1.25	5	0.11	0.03
10.00	10	0.08	1.40
5.00	10	0.12	0.85
2.50	10	0.02	0.35
1.25	10	0.08	0.13
10.00	20	0.26	1.76
5.00	20	0.19	0.90
2.50	20	0.04	0.32
1.25	20	0.07	0.18

Figure 12. Iso-contours of the wake vorticity for a filament resolution of 10.0° (upper), 2.5° (middle) and 1.25° (lower) and two different time-integration schemes: first-order explicit Euler (left) and fourth-order predictor–corrector Adams–Bashforth–Moulton (right). [Colour figure can be viewed at wileyonlinelibrary.com]

time schemes using a small-wake azimuthal discretization are almost inappreciable. In light of this results, the use of the Euler scheme is justified in all the simulations performed with a sufficiently small time step.

3.4. Validation of flow/aeroelastic solver coupling

The hybrid filament-mesh method is validated on two aeroelastic flow cases that are simulated using the aeroelastic coupling MIRAS-FLEX.[37] Here, the presented 3D viscous–inviscid panel method is coupled with a structural dynamics code FLEX5[38] that was originally designed to model the dynamic behavior of horizontal axis wind turbines. This method is advantageous to standard aeroelastic codes because of the more advanced aerodynamic model that can be seen as midway between blade element momentum and Navier–Stokes solvers. The structural behavior of the wind turbine is modeled using the principle of virtual work for a set of selected degrees of freedom (DOFs). Modal-shape functions are used for the deflections of the blades and tower, while stiff bodies connected by flexible hinges are used to model the nacelle, rotor shaft and hub. The aeroelastic solver contains a total of 28 DOFs where six of them describe the deformations of a

Table IV. Properties of the baseline land base NREL 5 MW wind turbine.[39]

Rated power	5 MW
Rotor orientation and configuration	Upwind and 3 blades
Airfoil profiles	40% to 21% DU and 18% NACA
Control	Variable speed and collective pitch
Rotor diameter	126 m
Hub diameter	3 m
Hub height	90 m
Overhang	5 m
Shaft tilt angle	5°
Pre-cone angle	2.5°
Drivetrain	High-speed, multiple-stage gearbox
Cut-in, rated and cut-out wind speed	3, 11.4 and 25 m s^1
Cut-in and rated rotor speed	6.9 and 12.1 rpm
Rated tip speed	80 m s^1
Rotor mass	110,000 kg
Nacelle mass	240,000 kg
Tower mass	347,460 kg

flexible foundation, not included in the present validation. MIRAS-FLEX coupling uses a predictor–corrector, loosely coupled, multi-rate methodology to transfer the aerodynamic loads as well as the deformations and velocities between the flow and the aeroelastic solvers. The present study focuses on the validation of the hybrid wake model in comparison with the direct-filament method. It is important to note here that the MIRAS-FLEX coupling has been previously validated against other aeroelastic tools, and it is not the aim of the present section to redo this validation. The wind turbine chosen for the present study is the land-based version of the National Renewable Energy Laboratory (NREL) 5 MW offshore baseline wind turbine[39] whose general properties are specified in Table IV.

In this case, the MIRAS-FLEX surface mesh consists of 20 span-wise and 150 chord-wise stations, with a total of 3000 cells, distributed using a cosine spacing in both the span-wise and chord-wise directions. The simulations have been performed for a short wake (five revolutions), in order to make the direct-filament method feasible and carry out a straight comparison between the two wake models. A total of 10,000 time steps are simulated with a time-step size of 0.02 s, which is defined in relation to the rotor aeroelastic properties.

The time step in MIRAS is dictated by the time step necessary to capture the wind turbine dynamics in a one-to-one coupling strategy.

Two test cases at a steady oncoming wind speed of 12 m s^1 with a constant rotational speed of 1.2671 rad s^1 have been selected to carry out the validation. First, a simple case with a 30° yaw misalignment between the rotor and the oncoming flow and no controller is selected. Secondly, a higher complexity case is defined with 30° yaw misalignment between the rotor and the oncoming flow, prescribed power-law wind shear of 0.2, tower-shadow effect, rotor tilt of 5.0° and a coning angle of −2.5°. With the wind turbine controller turned on, the controller can modify the generator speed as well as the blade pitch setting. In both test cases, the DOFs considered include first and second flap blade modes, first edge blade mode, first and second for-aft modes, first side–side tower modes and yaw and shaft torsion modes. The boundary layer is solved with free laminar to turbulent transition and a turbulent intensity of 0.1%.

The sensors selected for the analysis of the results are the blades thrust and torque, rotor thrust and torque, blade one flap-wise and edge-wise deflections, nacelle Y and Z position, tower torsion and tilt angle. This output sensors are selected to give an overall impression of the turbine performance during the MIRAS-FLEX simulation.

A visualization of the first case with the direct-filament and the hybrid method is shown in Figure 13. A detailed analysis of the selected output sensors is presented in Figure 14, where a very good agreement is observed for all quantities with the error committed by using the hybrid model is in the order of 0.1% in relation to the direct-filament predictions. To quantify the influence of the mesh size, simulations are performed with a finer mesh resolution, cell size of $D/80$. Comparison of rotor thrust, torque and nacelle X and Y positions are presented in Figure 14 with green lines. The already small error committed by hybrid method predictions with the standard mesh resolution of $D/40$ are clearly reduced and an excellent agreement with the direct-filament method is obtained.

The second case is shown in Figure 15. The analysis of the output sensors for this higher complexity case is presented in Figure 16, showing an almost identical picture as in the previous case. The direct-filament and the hybrid wake are in excellent agreement, with the error incurred by using the hybrid wake model being in the order of 0.1% for all analyzed quantities.
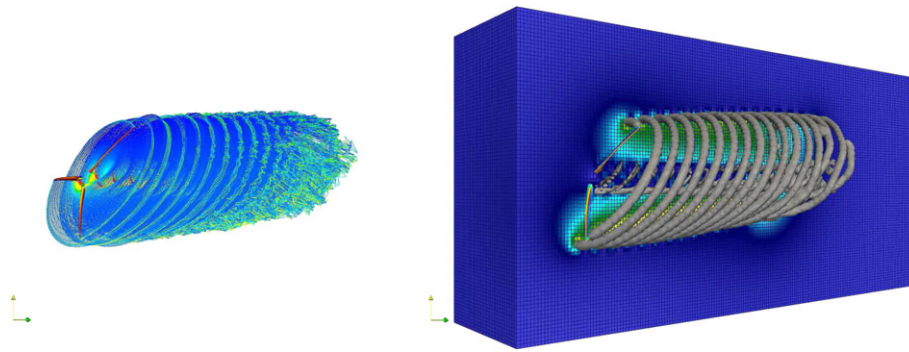
Figure 13. Aeroelastic MIRAS-FLEX simulations with 30° yaw: direct filament method (left) and hybrid method (right). [Colour figure can be viewed at wileyonlinelibrary.com]
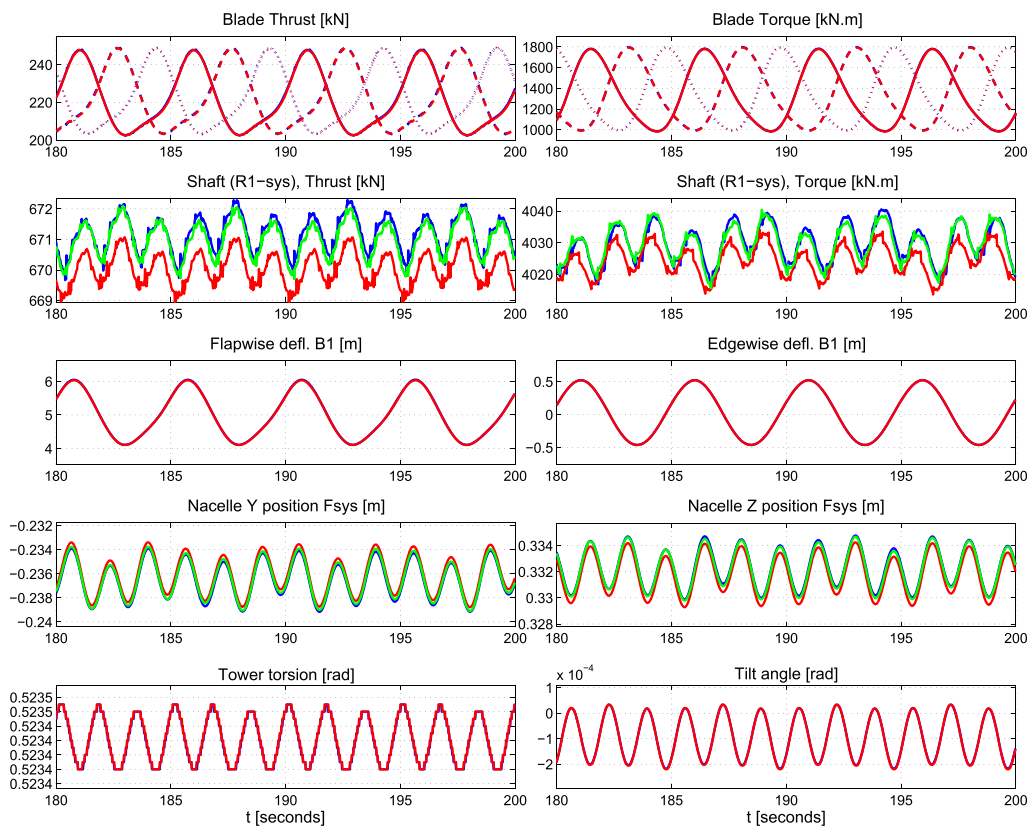

Figure 14. Aeroelastic MIRAS-FLEX simulations with 30° yaw 'few degrees of freedom'. ——, direct filament method; ——, hybrid method $dx = D/40$; ——, hybrid method $dx = D/80$. [Colour figure can be viewed at wileyonlinelibrary.com]

3.5. A comparison of the computational time between the direct and hybrid method

One of the main advantages of using the proposed hybrid method is the reduction in computational time as compared with the original direct-filament approach. In this section, the CPU time variation as function of different simulation parameters is analyzed.

First, the gain in CPU time obtained for different settings of the *startpmw* location in comparison with the direct filament simulation for the same azimuthal discretization is depicted in Figure 17. The results suggests that the CPU time is reduced as more filaments are handled by the filament-mesh calculations. This trend seems to be directly related to the wake
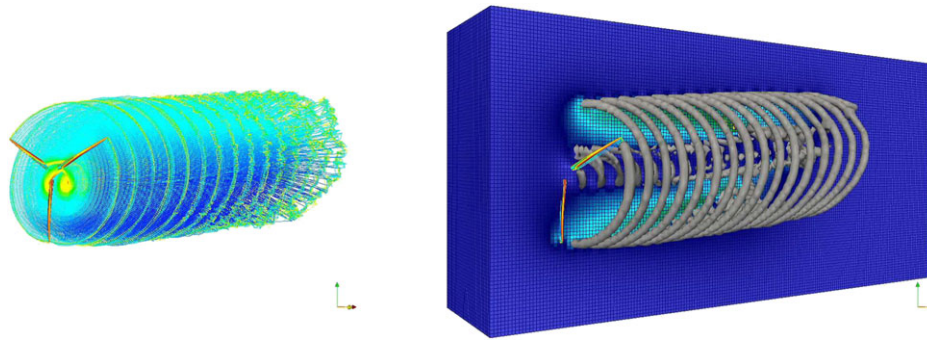
Figure 15. Aeroelastic MIRAS-FLEX simulations with 30° yaw, wind shear (0.2c) and tower shadow direct filament method (left) and hybrid method (right). [Colour figure can be viewed at wileyonlinelibrary.com]
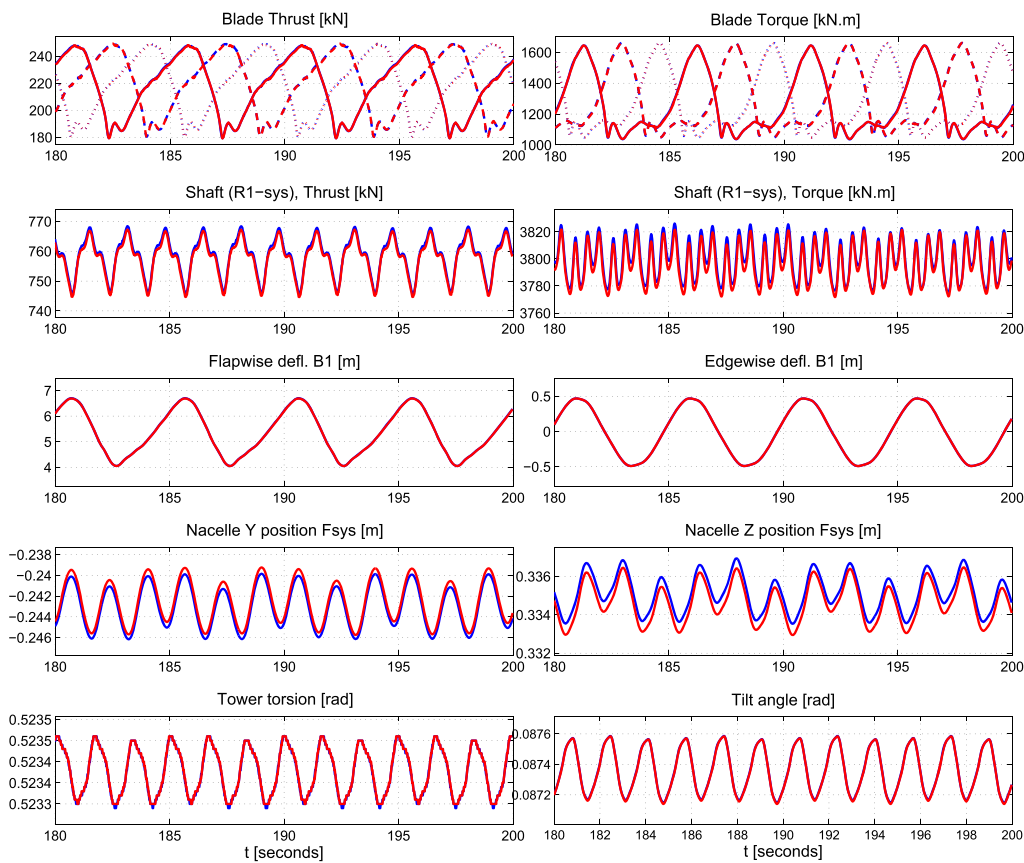

Figure 16. Aeroelastic MIRAS-FLEX simulations with 30° yaw, wind shear (0.2c) and tower shadow. ——, direct filament method; ——, hybrid method $dx = D/40$. [Colour figure can be viewed at wileyonlinelibrary.com]

azimuthal discretization, the more wake filaments are used to model the wake, the larger gain is obtained by using the hybrid wake approach.

In Table V, the influence in CPU time of the Cartesian mesh discretization is analyzed for a wake azimuthal discretization of 5°. The increase in CPU time because of a higher resolved mesh is almost negligible in comparison with the total CPU time.

The simulation time for the MIRAS-FLEX aeroelastic calculations is presented in Table VI. Here, the *startpmw* location is set to 4.2° with a mesh resolution of $D/40$. A number of 10,000 time steps are simulated in all cases, with the time discretization set to 0.02 s. In order to reduce the number of direct interactions between the blade panels and the wake
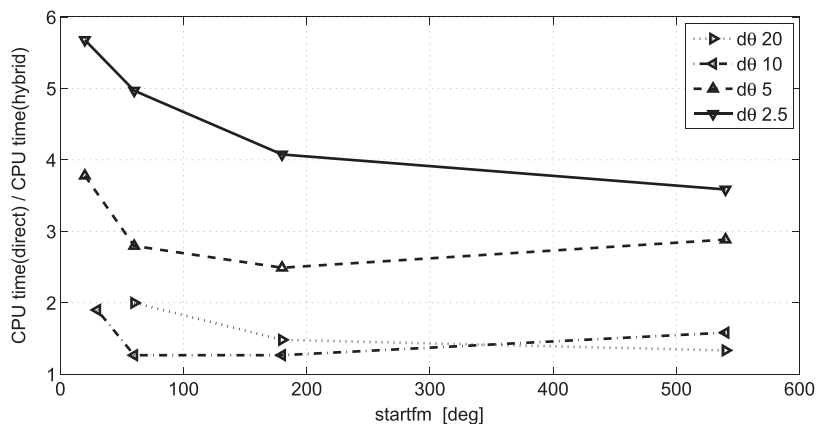
Figure 17. CPU time study on MEXICO rotor, MIRAS simulations at a wind speed of 15 m s[1], influence of particle wake start location (*startpmw*) and the filament resolution ($d\theta$).

Table V. CPU time study on MEXICO rotor, influence of mesh spacing (h). MIRAS simulations at a wind speed of 15 m s[1], $d\theta = 5.0$ [°] and 20 wake revolutions.

Mesh resolution	Wall time (h)	Number of processors (—)	CPU time (h)
$D/10$	6.60	40	264
$D/20$	6.60	40	264
$D/40$	7.15	40	286
$D/80$	7.50	40	300

Table VI. CPU time study on NREL 5 MW rotor, MIRAS-FLEX simulations for case number one (30° yaw), 10,000 time steps, $d\theta = 1.4°$ and $dt = 0.02$ s. The CPU time for the direct-filament method with 30 wake revolutions is obtained by linear extrapolation.

Wake revolutions	Method	Wall time (h)	Number of processors (—)	CPU time (h)
2.35	Hybrid	14.50	40	580
2.35	Direct	27.00	200	5400
5.10	Hybrid	17.60	40	704
5.10	Direct	70.50	200	14,100
7.80	Hybrid	20.00	40	800
7.80	Direct	134.25	200	26,850
30.00	Hybrid	28.50	40	1140
30.00	Direct	—	—	131,683

filaments, the influence of the blade is truncated one radius downstream the rotor plane. This truncation showed very small effect in the rotor integral forces as well as wake velocities. Moreover, the CPU time is drastically reduced since the direct one-to-one panel to filament interaction is confined to a certain distance. An excellent speedup of more than a factor of 30 is achieved for the 7.8 wake revolutions case. Extrapolating the results for a 30 revolutions wake, an approximate speedup of 115 is obtained.

4. CONCLUSION

A new hybrid filament-mesh method for efficiently calculating the interactions of wind turbine wakes has been introduced and validated. The model combines a direct-filament approach to calculate the vortex interactions in the vicinity of the wind turbine rotor, with a filament-mesh method used to calculate the vortex interactions of the further downstream wake. The new method has been validated against the original direct-filament method for a large variety of cases.

It was shown that the implementation of the hybrid filament-mesh method did not compromise the accuracy of the simulations. For the benchmark cases, it was shown that a mesh resolution below $D/20$ is sufficient to predict the thrust and torque on the rotor with an error less than 1.0% compared with the direct method. A finer resolution is however needed for accurately simulating the flow in the near-wake region.

The location of the transition between using the direct filament method and the filament-mesh method to calculate the vortex interactions was investigated. It was here shown that in simulations using a fine filament discretization, the transition to the filament-mesh method could be performed at an earlier point in the wake that may be utilized in order to increase the efficiency of the computations.

A short study regarding the time-integration scheme was presented. Here, it was shown that a simple Euler method can indeed be used in simulations with small but feasible time-step size to accurately predict the thrust and torque on the rotor and near-wake behavior.

Finally, an overall reduction in the CPU time was achieved by using the hybrid filament-mesh method. A speedup of more than 30 times was shown in the benchmark cases, which by using a linear extrapolation, corresponds to a speedup of more than 115 for a wake of 30 revolutions. The overall assessment is that the hybrid filament-mesh implementation offers an attractive method that gives a significant speedup in the computational time while still maintaining the accuracy of the method.

ACKNOWLEDGEMENT

REFERENCES

1. Sessarego M, Ramos-García N, Yang H, Shen WZ. Aerodynamic wind-turbine rotor design using surrogate modeling and three-dimensional viscous–inviscid interaction technique. *Renewable Energy* 2016; **93**: 620–635. https://doi.org/10.1016/j.renene.2016.03.027.
2. Hansen MOL. *Aerodynamics of Wind Turbines* (2nd ed). Earthscan, 2008.
3. Balleur JCL. Strong matching method for computing transonic viscous flows including wakes and separations. *La Recherche Aérospatiale* 1981; **3**: 21–45.
4. Brune GW, Rubbert PE, Nark TC. A new approach to inviscid flow/boundary layer matching. *AIAA-74-601* 1974.
5. Calvert WJ. An inviscid–viscous interaction treatment to predict the blade-to-blade performance of axial compressors with leading-edge normal shock waves. *ASME paper No 82-GT-135* 1982.
6. Drela M, Giles MB. Viscous–inviscid analysis of transonic and low Reynolds number airfoils. *AIAA journal* 1987; **25**: 1347–1355.
7. Sørensen JN. Prediction of separated flow past airfoil using viscous–inviscid interaction technique. *La Recherche Aerosptatiale* 1988; **3**: 1–11.
8. Veldman AEP, Carter JPF. New quasi-simultaneous method to calculate interacting boundary layers. *AIAA Journal* 1981; **19**: 79–85.
9. Bampalas N, Graham JMR. Aerodynamic rotor model for unsteady flow and wake impact. *Oldenburg University Workshop*, 2008.
10. Bareiss R, Wagner S. The free wake/hybrid wake code ROVLM—a tool for aerodynamic analysis of wind turbines. *European Community Wind Energy Conference* 1993.
11. Pesmajoglou SD, Graham JMR. Prediction of aerodynamic forces on horizontal axis wind turbines in free yaw and turbulence. *Journal of Wind Engineering and Industrial Aerodynamics* 2000; **86**.
12. Roura M, Cuerva A, Sanz-Andrés A, Barrero-Gil A. A panel method free-wake code for aeroelastic rotor predictions. *Wind Energy* 2009; **13**: 357–371.
13. Voutsinas SG. Theoretical and numerical analysis of three dimensional subsonic inviscid flows. PhD Thesis, 1990.
14. Voutsinas SG. Vortex methods in aeronautics: how to make things work. *International Journal of Computational Fluid Dynamics* 2006; **20-1**: 3–18.
15. Voutsinas SG, Belessis MA, Huberson S. Dynamic inflow effects and vortex particle methods. *European Community Wind Energy Conference*, Lübeck-Travemünde, Germany, 1993.
16. Whale J, Anderson CG, Bareiss R, Wagner S. An experimental and numerical study of the vortex structure in the wake of a wind turbine. *Journal of Wind Engineering and Industrial Aerodynamics* 2000; **84**: 1–21.
17. Carrier J, Greengard L, Rokhlin V. A fast adaptive multipole algorithm for particle simulations. *SIAM Journal on Scientific and Statistical Computing* 1988; **9**: 669–686.
18. Barnes J, Hut P. A hierarchical $O(N \log N)$ force-calculation algorithm. *Nature* 1986; **324**: 446–449.

19. Hockney RW, Eastwood JW. *Computer Simulation Using Particles* (2nd ed). Institute of Physics Publishing: Bristol, PA, USA, 1988.

20. Hejlesen MM. A high order regularisation method for solving the Poisson equation and selected applications using vortex methods, *Ph.D. Thesis*, 2016.

21. Hejlesen MM, Rasmussen JT, Chatelain P, Walther JH. A high order solver for the unbounded Poisson equation. *Journal of Computational Physics* 2013; **252**: 458–467.

22. Hejlesen MM, Rasmussen TJ, Chatelain P, Walther JH. High order Poisson solver for unbounded flows. *Procedia IUTAM* 2015; **18**: 56–65.

23. Ramos-García N, Shen WZ, Sørensen JN. Three-dimensional viscous–inviscid coupling method for wind turbine computations. *Published online in Wind energy* 2014. https://doi.org/10.1002/we.1821.

24. Ramos-García N, Shen WZ, Sørensen JN. Validation of a three-dimensional viscous–inviscid interactive solver for wind turbine rotors. *Renewable Energy* 2014; **70**: 78–92. https://doi.org/10.1016/j.renene.2014.04.001.

25. Katz J, Plotkin A. *Low Speed Aerodynamics: From Wing Theory to Panel Methods* 2nd ed. McGraw-Hill, 1977.

26. Scully MP. Computation of helicopter rotor wake geometry and its influence on rotor harmonic airloads. PhD Thesis, Massachusetts Institute of Technology. Dept. of Aeronautics and Astronautics, 1975.

27. Leishman JG, Bhagwat MJ, Bagai A. Free-vortex filament methods for the analysis of helicopter rotor wakes. *Journal of Aircraft* 2002; **39**: 759–775.

28. Ananthan S, Leishman JG. Role of filament strain in the free-vortex modeling of rotor wakes. *Journal of the American Helicopter Society* 2004; **9**: 176–191.

29. Squire HB. The growth of a vortex in turbulent flow. *Aeronautical Quarterly* 1965; **16**: 302–306.

30. Monaghan JJ. Extrapolating B splines for interpolation. *Journal of Computational Physics* 1985; **60**: 253–262.

31. Lighthill MJ. On displacement thickness. *Journal of Fluid Mechanics* 1958; **4**: 383–392.

32. Ramos-García N, Shen WZ, Sørensen JN. A strong viscous–inviscid interaction model for rotating airfoils. *Published online in Wind energy* 2013. https://doi.org/10.1002/we.1677.

33. Thwaites B. Approximate calculation of the laminar boundary layer. *The aeronautical Quarterly* 1949; **1**: 245–280.

34. Mack LM, *Transition and laminar instability*, Technical Report JPL PUBLICATlON 77-15, National Aeronautics and Space Administration, Jet Propulsion Laboratory, 1977.

35. Scheepers JG, Snel H, *Model experiments in controlled conditions final report*, Technical Report ECN-E–07-042, The Energy Research Center of the Netherlands, 2007.

36. Scheepers JG, Boorsma K, Cho T, Gomez-Iradi S, Schaffarczyk P, Jeromin A, Shen WZ, Lutz T, Meister K, Stoevesandt B, Schreck S, Micallef D, Pereira R, Sant T, Madsen HA, Sørensen N, *Final report of IEA Task 29, Mexnext (phase 1): analysis of Mexico wind tunnel measurements*, Technical Report ECN-E–12-004, The Energy Research Center of the Netherlands, 2012.

37. Sessarego M, Ramos-García N, Shen WZ, Sørensen JN. Development of an aero-elastic code based on three-dimensional viscous–inviscid method for wind turbine computations. *Submitted to Wind energy* 2016.

38. Øye S. FLEX4 simulation of wind turbine dynamics. *Proceedings of 28th IEA Meeting of Experts Concerning State of the Art of Aeroelastic Codes for Wind Turbine Calculations, International Energy Agency, Lyngby* 1996.

39. Jonkman J, Butterfield S, Musial W, Scott G, *Definition of a 5-MW reference wind turbine for offshore system development*, Technical Report DOI:10.2172/947422, National Renewable Energy Laboratory, NREL, 2009.